

Article

Facile Method to Prepare pH-Sensitive PEI-Functionalized Carbon Nanotubes as Rationally Designed Vehicles for Non-Steroidal Anti-Inflammatory Drugs (NSAIDs) Delivery

Vassilis Tangoulis ^{1,*}, Nikolia Lalioti ¹, John Parthenios ², Nathan Langford ³,
Eugenia Valsami-Jones ³, Chrisoula Kakoulidou ⁴, George Psomas ⁴ and Vlasoula Bekiari ⁵

¹ Department of Chemistry, University of Patras, GR-26504 Patras, Greece; lali@upatras.gr

² Foundation for Research and Technology, Hellas (FORTH), Institute of Chemical Engineering Sciences (ICE/HT), P.O. Box 1414, GR-26504 Patras, Greece; jparthen@iceht.forth.gr

³ School of Geography, Earth and Environmental Sciences, University of Birmingham, Edgbaston, Birmingham, UK; nxl428@student.bham.ac.uk (N.L.); E.ValsamiJones@bham.ac.uk (E.V.-J.)

⁴ Department of General and Inorganic Chemistry, Faculty of Chemistry, Aristotle University of Thessaloniki, P.O. Box 135, GR-54124 Thessaloniki, Greece; ckakouli@gmail.com (C.K.); gepsomas@chem.auth.gr (G.P.)

⁵ Department of Crop Science, University of Patras, 30200 Messolonghi, Greece; bbekiari@upatras.gr

* Correspondence: vtango@upatras.gr; Tel.: +30-2610-9977-039

Received: 21 September 2020; Accepted: 3 October 2020; Published: 7 October 2020



Abstract: A new pH-sensitive system designed for drug-delivery purposes and based on functionalized multiwall magnetic carbon nanotubes (Mag-CNTs) was synthesized for the effective incorporation of non-steroidal anti-inflammatory drugs (NSAIDs), aiming at drug release in characteristic acidic conditions close to the actual conditions of inflamed tissues. Cationic hyperbranched polyethyleneimine (PEI) was immobilized on the surface of Mag-CNTs via electrostatic interactions between the positively charged protonated amines within the polymer and the carboxyl groups on the chemically oxidized Mag-CNT surface. The addition of the NSAID with a carboxylate donor, Naproxen (NAP), was achieved by indirect coupling through the amino groups of the intermediate linker PEI. FT-IR, Raman, and UV-vis spectroscopy were employed to fully characterize the synthesized nanocarrier and its functionalization procedure. The interaction of the designed nanocarrier with bovine serum albumin (BSA) was studied in vitro by fluorescence emission spectroscopy while its in vitro interaction with calf-thymus (CT) DNA was monitored by UV-vis spectroscopy and viscosity measurements and via competitive studies with ethidium bromide. The calculated binding constants were compared to those of free NAP revealing a higher binding affinity for BSA and CT DNA. Finally, drug-release studies were performed, revealing that the electrostatic linkage ensures an effective release of the drug in the acidic pH typical of inflamed cells, while maintaining the multiwall nanotubes (MWNTs)-drug conjugates stable at the typical bloodstream.

Keywords: NSAID; Mag-CNTs; drug-release; PEI-CNTs; DNA; drug-delivery

1. Introduction

A fascinating category of nanomaterials possessing unique physical, chemical, and physiological properties is carbon nanotubes (CNTs) [1–6]. Their chemical modification has attracted increasing attention over recent years in order to improve their solubility and compatibility, tailor their structures and properties, and open a whole new world of novel CNT-based nanostructures and

nanomaterials [7–11]. In a parallel manner, the use of nanotechnology in the field of pharmaceuticals and drug-delivery has remarkably grown over the last few years, giving “birth” to a new term developed on the basis of this technology—nanopharmaceuticals. As a matter of fact, CNTs possess many intriguing features that make them attractive drug-delivery carriers such as: (a) An enhanced permeability and retention (EPR) effect. Nanocarriers such as nanoparticles (NPs), liposomes, and CNTs, experience a higher accumulation in tumor tissues as compared to normal tissues because of the poorly formed blood and lymphatic vessels that supply rapidly proliferating tumors [12]. The EPR effect empowers CNTs to transport chemotherapeutic agents preferentially to tumor sites [13]. (b) Trans-membrane penetration and intracellular accumulation through the needle-like shape of CNTs via the “nanoneedle” mechanism [14] and/or energy-dependent endocytic pathways [15]. (c) Extraordinary ability for drug-loading and efficient attachment onto the surface or within the interior core of CNTs [16–18]. The functionalization of CNTs involves three different approaches: (i) the attachment [19,20] of molecules through covalent bonding; (ii) the functionalization of molecules on the graphitic surface by an adsorption mechanism [21]; (iii) the encapsulation of molecules in the empty cavity of the nanotubes.

Considering the non-covalent functionalization of CNTs, molecules containing aromatic groups are adsorbed on the conjugated surface of the nanotubes mainly through π - π interactions [22]. CNTs are excellent candidates for the role of carriers mainly because their inner space can be filled with nanoparticles or molecules while the graphitic wall can be further functionalized in order to enrich biocompatibility, to succeed biodegradation [23], and to convey novel functions for targeting [24] or imaging purposes [25–27]. In comparison with the non-covalent functionalization of CNTs, the covalent one is clearly more accurate, better controllable and robust. The conjugates of non-covalent functionalized CNTs are easily dissociated in biological fluids, creating more concerns about potential hazardous effects. One of the main reasons for this is the undesired exchange of the detached molecules with serum proteins after administration. Nevertheless, it seems that, for certain cases, the non-covalent functionalization of CNTs is more advisable since the experimental conditions are ideal to maintain the physical properties (structural, electrical and optical) of the CNTs as well as the properties of the adsorbed molecules. On the other hand, the covalent grafting of various substances on the graphitic sidewalls dramatically changes the conjugated π -electron framework of CNTs mainly due to the induced rehybridization (from sp^2 to sp^3) of the derivatized carbon atoms accompanied by a drastic change of their optical-electrical properties.

In special cases, CNTs can also reveal fascinating magnetic properties (Mag-CNTs) which derive from the metal catalyst impurities entrapped at the CNT extremities during their manufacture. These Mag-CNTs can be used as magnetic resonance imaging (MRI) contrast agents even with low metal impurities (>2% iron, nickel), having a significant effect on the observed ^1H transverse ($1/T_2$) relaxation rate of water [28]. Mag-CNTs can offer a plethora of capabilities in clinical uses such as: (a) contrast agents in MRI; (b) drug carriers effectively surpassing certain limitations that drugs undergo mainly because of the decreasing efficacy and rather poor cytotoxicity and/or targeting [29].

The main objective of designing “smart” Mag-CNTs drug-carriers is the selective targeting of specific biological entities by avoiding “barriers” inside the body. These in vivo barriers: (a) shield the body against external species intrusion; (b) limit the movement of Mag-CNTs; (c) enter severe changes to the surface and their magnetic properties; (d) result in an early uptake by cells after biochemical signaling induces a negative host response before the Mag-CNTs reach the target tissue [30,31]. A representative example is the blood-driven agglomeration of Mag-CNTs when entering the body through intravascular administration. Until recently, intermediate biocompatible coatings using polyethyleneglycol (PEG) co-polymers, polyethylene imine (PEI) molecules, dextrans, liposomes, etc. have been studied in depth regarding case of the indirect drug addition on as-prepared Mag-CNTs [29].

Non-steroidal anti-inflammatory drugs (NSAIDs) are perhaps the most prescribed drug groups [32–36] widely used in drastic inflammatory conditions and chronic inflammatory diseases. Despite their wide usage, it has been shown that the long-term use of NSAIDs is accompanied by a high risk of gastrointestinal bleeding causing a significant reduction in current therapies mainly

because drugs must frequently be administered at suboptimal doses to reduce cytotoxicity. A plethora of strategies have been employed over the last 50 years for the development of NSAIDs that spare the gastrointestinal tract [32–36] without any promising results. A possible answer to this problem is the use of nanoplateforms as controlled release systems, developed the last decade due to advances made in nanoscience and nanotechnology. The main advantages of these systems are the following: (a) they maintain the drug concentration in the body releasing only in the injured cells; (b) increase the overall therapeutic efficiency of the drug and (c) all physical properties such as size, porosity, geometry and surface functionalization can be controlled at the nanoscale level.

Herein, we present the effective attachment of Naproxen (NAP), a carboxylate NSAID, commonly used for the treatment of inflammations and pain of various wounds on the surface of PEI-functionalized carboxylated Mag-CNTs. A facile method is employed for the preparation of the Mag-CNTs@PEI@NAP carriers based on the indirect coupling of NAP through the amino groups of the intermediate linker PEI. The interaction of the produced nanocarrier with bovine serum albumin (BSA) was studied *in vitro* along with its interaction to bind to calf-thymus (CT) DNA. The calculated binding constants revealed a higher binding affinity for BSA and CT DNA than free NAP. Finally, drug-release studies were performed, revealing an effective release of the drug in acidic conditions.

2. Materials and Methods

2.1. General Synthetic Remarks

Mag-CNTs (product name: NTX4, multiwall carbon nanotubes up to 94% purity, external diameter 6–15 nm, internal diameter 1–6.5 nm, length > 10 μm , less than 6% impurities including: amorphous content less than 1%, and Fe < 1.5%) were obtained from Nanothinx S.A. (Rio Patras, Greece). Samples were filtered by employing a vacuum filter funnel of pore size number 3, and either hydrophobic polytetrafluoroethylene (PTFE) membrane filters (0.45 μm pore size) or cellulose nitrate membrane filters (0.45 μm pore size). 1-(3-Dimethylaminopropyl)-3-ethylcarbodiimide hydrochloride, (EDC, >98.0%, Triethylamine (Et₃N, \geq 99.5%) and N-hydroxysuccinimide (NHS, 98.0%), trisodium citrate, NaCl, calf-thymus (CT) DNA, bovine serum albumin (BSA) and ethidium bromide (EB) were purchased from Sigma-Aldrich and (S)-(+)-2-(6-methoxy-2-naphthyl)propionic acid (NAP) and poly(ethyleneimine) solution (PEI, Mn ~1800) from Alfa Aesar.

2.2. Shortening and Functionalization of Mag-CNTs (NL002)

Mag-CNTs were shortened employing an ultrasonic processor (24 kHz, 400 W, UP400S Hielscher). A total of 3.0 g of Mag-CNTs was suspended in 400 mL 3DH₂O employing ultrasonication in full power and a time duration close to 4 h. The sample was filtered under vacuum using a 0.47 μm nylon membrane filter (Isopore Millipore) and dried in the oven for 12 h at 110 °C. Scanning electron microscopy (SEM) of the Mag-CNTs revealed a direct relation of the ultrasonication time and the final length of the carbon material. Ultrasonication in full power for 4 h showed a length range between 500 and 700 nm, while for 2 h the length range was between 1.5 and 2.0 μm .

For the carboxylated Mag-CNTs, 2.0 g of Mag-CNTs was dispersed in 100 mL HNO₃ 65% employing an ultrasonic processor for 10 min, 180 W and the solution was stirred on a hot plate (mechanically) at 90 °C for 3.5 h. Afterwards, the heating was switched off and the solution was continuously stirred overnight. The sample was filtered under vacuum using a 0.47 μm nylon membrane filter under 3DH₂O, reflux up to a pH between 7 and 8 and dried in the oven for 12 h at 110 °C.

For the deprotonation of the carboxylic groups, a two-step procedure was carried out. Firstly, the sample was dispersed in 80 mL of an aqueous solution NaOH 10% *w/w* under ultrasonication (5 min at 210 W). Then, the solution was vacuum-filtered and, under stirring, dispersed in 100 mL of an aqueous solution of NaOH 10% *w/w*, and stirred for 30 min. This procedure was repeated one more time and finally the sample was vacuum-filtered using a 0.45 μm polycarbonate membrane filter under 3DH₂O maintaining the pH between 7 and 8, and dried overnight at 110 °C.

2.3. PEI-Functionalization of Carboxylated Mag-CNTs (NL003)

A total of 40 mg of the carboxylated Mag-CNTs (sample name: NL002) was suspended in 20 mL of chloroform. This mixture was then placed in a bath sonicator for 30 min to break up any of the larger aggregates. Concurrently, 4 mL of the PEI solution (1.08 g/mL) was added to 16 mL of 3DH₂O to a total volume of 20 mL at a concentration of 200 mg of PEI/mL. These two solutions were then combined in a suitable beaker. This beaker was then covered and placed under the horn sonicator at 20% power for 3 h while undergoing slight magnetic stirring. After this period, the mixture was heated on a hotplate to evaporate any excess chloroform, taking care not to raise the temperature above 80 °C. Once the chloroform had been taken off, the Mag-CNTs@PEI (code name: NL003) was subjected to centrifugation to remove large aggregates and the supernatant vacuum was filtered through a 0.45 micrometer PTFE membrane, while being continuously washed with ethanol. The centrifugation step is very important since the agglomeration of carbon nanotubes as a result of the van der Waals interactions tends to increase cytotoxicity. After 3 washes with ethanol, the membranes were left to dry overnight in a warm oven.

2.4. Indirect Coupling of NAP on Mag-CNTs@PEI (NL004)

A total of 20 mg of Mag-CNTs@PEI (sample name: NL003) was suspended in 6 mL of 3DH₂O and placed in a water bath sonicator for 30 min. During a second step, a fresh solution of 48 mg of EDC, 108 mg NAP, and 0.1 mL of Et₃N to 5 mL of chloroform was prepared. These two solutions were then combined and placed under the horn sonicator for 4 min at 40% power to ensure good dispersion. This mixture was then covered and magnetically stirred for 24 h. After stirring, the solution was again heated to remove any excess of chloroform. As before, care was taken not to let the solutions temperature rise above 80 °C and was then filtered in the same way through a 0.45 micrometer PTFE membrane while being washed with ethanol. The filter paper was then removed and left to dry before collecting the **Mag-CNTs@PEI@NAP** (NL004) product.

2.5. FT-IR/UV-Vis Spectra

Infrared spectra (400–4000 cm⁻¹) were recorded on a Nicolet FT-IR 6700 spectrometer with samples prepared as a KBr disk while the Attenuated Total Reflection (ATR) spectra were recorded on a “Bruker Optics” Alpha-P Diamond ATR Spectrometer of Bruker Optics GmbH”. UV-vis spectra were recorded in solution at concentrations in the range 10⁻⁵–10⁻³ M on a Hitachi U-2001 dual beam spectrophotometer. Viscosity experiments were carried out using an ALPHA L Fungilab rotational viscometer equipped with an 18 mL LCP spindle. Fluorescence spectra were recorded in solution on a Hitachi F-7000 fluorescence spectrophotometer. The C, H, and N elemental analysis was performed on a Perkin-Elmer 240B elemental analyzer.

2.6. Raman Measurements

The acquisition of the Raman spectra was obtained with a Renishaw InVia Reflex at 785 nm (1.58 eV). The laser power was kept below 1.6 mW in order to minimize the laser-heating effects on the probed materials while the laser was focused on the sample using a ×100 objective.

2.7. Drug-Release Protocol

The emission characterization of NL004 was recorded on a Cary Eclipse emission spectrophotometer. The drug-release behavior was investigated according to the following procedure: 1 mg of NL004 was dispersed in 5 mL of three buffered solutions (pH = 4.1, 6.8 and 10.1) under stirring at room temperature. At predetermined time intervals the solution was transferred in a cuvette and the emission intensity of NAP at 357 nm was recorded. The cumulative release (%) was expressed as:

$$\text{Cumulative release (\%)} = \frac{W_t}{W_{drug}} \times 100 \quad (1)$$

where W_t and W_{drug} indicate the weight of drug released from the hybrid material at time t , and the total amount of loaded drug, respectively [37]. W_t and W_{drug} were calculated from the calibration curve of free naproxene emission intensity at various concentrations, under the same excitation and emission wavelengths.

2.8. Preparation of CT DNA Solution for DNA-Binding Studies

The stock DNA solution was prepared by diluting CT DNA to buffer (containing 150 mM NaCl and 15 mM trisodium citrate at pH 7.0); the resultant solution was stirred at 4 °C for three days, and kept at 4 °C up to two weeks. The UV spectrum of the stock CT DNA solution was recorded giving a ratio of UV absorbance at 260 and 280 nm (A_{260}/A_{280}) equal to 1.89, showing that the DNA was sufficiently free of protein [38]. The concentration of the CT DNA solution was determined via the UV absorbance at 260 nm with a 1:20 dilution using $\epsilon = 6600 \text{ M}^{-1}\text{cm}^{-1}$ [39].

2.9. Albumin and DNA-Binding Studies

In order to evaluate the biological behavior of NL004, a DMSO solution was used. Mixing this solution with the aqueous buffer DNA/albumin-containing solutions used in the studies never exceeded 5% DMSO (v/v) in the final solution, which was needed due to low aqueous solubility. The biological behavior of free NAP has been previously reported [40,41]. Control experiments with DMSO were performed and no changes in the spectra of the albumins or CT DNA were observed. All studies were performed at room temperature.

The albumin-binding was studied by tryptophan fluorescence quenching experiments using bovine serum albumin (BSA, 3 μM) in buffer (containing 15 mM trisodium citrate and 150 mM NaCl at pH 7.0). The quenching of the emission intensity of tryptophan residues of BSA at 343 nm was monitored using NL004 as the quencher [42]. The fluorescence emission spectra of BSA in the presence of the solution were recorded in the range 300–500 nm with an excitation wavelength (λ_{ex}) of 295 nm. The fluorescence emission spectra of NL004 in DMSO/buffer solutions did not exhibit any appreciable fluorescence emission band under the same experimental conditions (i.e., $\lambda_{\text{ex}} = 295 \text{ nm}$). The influence of the inner-filter effect on the measurements [43] was evaluated by Equation (S1) and did not affect the measurements. The Stern–Volmer and Scatchard equations (Equations (S2)–(S4)) and graphs were used in order to study the interaction of NL004 with BSA and calculate the Stern–Volmer constant K_{SV} (in M^{-1}), the SA-quenching constant k_q (in $\text{M}^{-1}\text{s}^{-1}$), the SA-binding constant K (in M^{-1}) and the number of binding sites per albumin n [44].

The interaction of NL004 with CT DNA was studied directly by UV–vis spectroscopy and viscosity measurements and indirectly via EB-competitive studies. UV–vis spectroscopy was employed to investigate the possible binding modes to CT DNA and to calculate the DNA-binding constant (K_b). Therefore, the UV–vis spectra of CT DNA were recorded for a constant DNA-concentration in the presence of NL004 at increasing [compound]/[DNA] mixing ratios ($=r$). The DNA-binding constant of NL004, K_b (in M^{-1}), was determined by the Wolfe–Shimer equation (Equation (S5)) [45] and the plots $[\text{DNA}]/(\epsilon_A - \epsilon_f)$ versus [DNA] when the UV–vis spectra of the compound were recorded in the presence of DNA for diverse r values.

The viscosity of DNA ([DNA] = 0.1 mM) in buffer solution (150 mM NaCl and 15 mM trisodium citrate at pH 7.0) was measured in the presence of increasing amounts of NL004 (up to the value of $r = 0.40$). All measurements were performed at room temperature. The obtained data are presented as $(\eta/\eta_0)^{1/3}$ versus r , where η is the viscosity of DNA in the presence of the compound, and η_0 is the viscosity of DNA alone in buffer solution.

The competitive study of NL004 with EB was investigated by fluorescence emission spectroscopy in order to examine the ability of NL004 to displace EB from its DNA–EB conjugate. The DNA–EB conjugate was prepared by adding 20 μM EB and 26 μM CT DNA in buffer (150 mM NaCl and 15 mM trisodium citrate at pH 7.0). The possible intercalating effect of NL004 was studied by adding a certain amount of NL004 stepwise into a solution of the DNA–EB complex. The influence of the

addition of NL004 to the DNA–EB solution was obtained by recording the changes of fluorescence emission spectra with $\lambda_{\text{ex}} = 540$ nm. NL004 did not show any fluorescence emission bands at room temperature in solution or in the presence of DNA or EB under the same experimental conditions ($\lambda_{\text{ex}} = 540$ nm); therefore, the observed quenching was attributed to the displacement of EB from its EB–DNA conjugate. The value of the Stern–Volmer constant (K_{SV} , in M^{-1}) was calculated according to the linear Stern–Volmer equation (eq. S2) [46] and the plot I_0/I versus $[Q]$. Taking $\tau_0 = 23$ ns as the fluorescence lifetime of the EB–DNA system, ref. [47] the quenching constant (k_q , in $M^{-1}s^{-1}$) for NL004 was calculated according to eq. S3.

3. Results

3.1. Synthetic Considerations

Mag-CNTs could be functionalized with groups containing oxygen, such as $-\text{OH}$ and $-\text{COOH}$, mainly at the outer sidewall ends where several defects are introduced during the oxidation procedure. These oxygen-containing groups could be used for the reaction to conjugate other functional groups (Figure 1). The functionalization of the Mag-CNTs was confirmed by FT-IR spectroscopy (Figure S1) where characteristic absorption peaks at 3400 cm^{-1} , and $(1615, 1117)\text{ cm}^{-1}$ corresponded to the hydroxyl and carbonyl groups conjugated to the $\text{C}=\text{C}$ and the $\text{C}-\text{O}$ stretching vibration, respectively. In our experimental protocol, PEI, a cationic polymer in branched form, was used to provide a high density of cations on the surface of the carbon nanotubes. Despite its extensive applications, PEI is cytotoxic and chemical modification is required to improve its properties as a transfection reagent [23,26–28]. The direct functionalization of the carboxylated carbon nanotubes with PEI would not only increase their biocompatibility but also reduce the toxicity of the PEI. In spite of this, the conclusions on the toxicity and transfection efficiency of PEI-functionalized carbon nanotubes in comparison to pure PEI that have appeared in the literature are quite contradictory [48,49]. In our study, the branched PEI~1.8 kDa readily adsorbed on the surface of the carbon nanotubes through a biphasic procedure (Figure 1) and rendered a hydrophilic surface (it is possible for every third atom of the polymer backbone to be positively charged). In the FT-IR spectrum of the PEI-functionalized carbon nanotube (NL003), the characteristic intense peak at 3360 cm^{-1} was assigned to the $N-H$ of PEI (Figure S1). Additionally, the band at 1650 cm^{-1} of the NL003 resulted from the bending of primary amine groups ($-\text{NH}_2$), which was incorporated into a broad band at 1580 cm^{-1} in PEI [50]. The amino groups of PEI were further exploited for the covalent attachment of the carboxylate drug (NAP) through an amide formation. After the reaction with NAP, the cytotoxicity of PEI can be safely assumed to be decreased due to the reduction in PEI's cationic density. In the FT-IR spectrum of the PEI-NAP-functionalized carbon nanotube (NL004) the characteristic vibrations of the amide formation between the $-\text{NH}_2$ of the PEI and the $-\text{COOH}$ of the NAP were observed ($\sim 1640\text{ cm}^{-1}$) and proved the successful reaction [51].

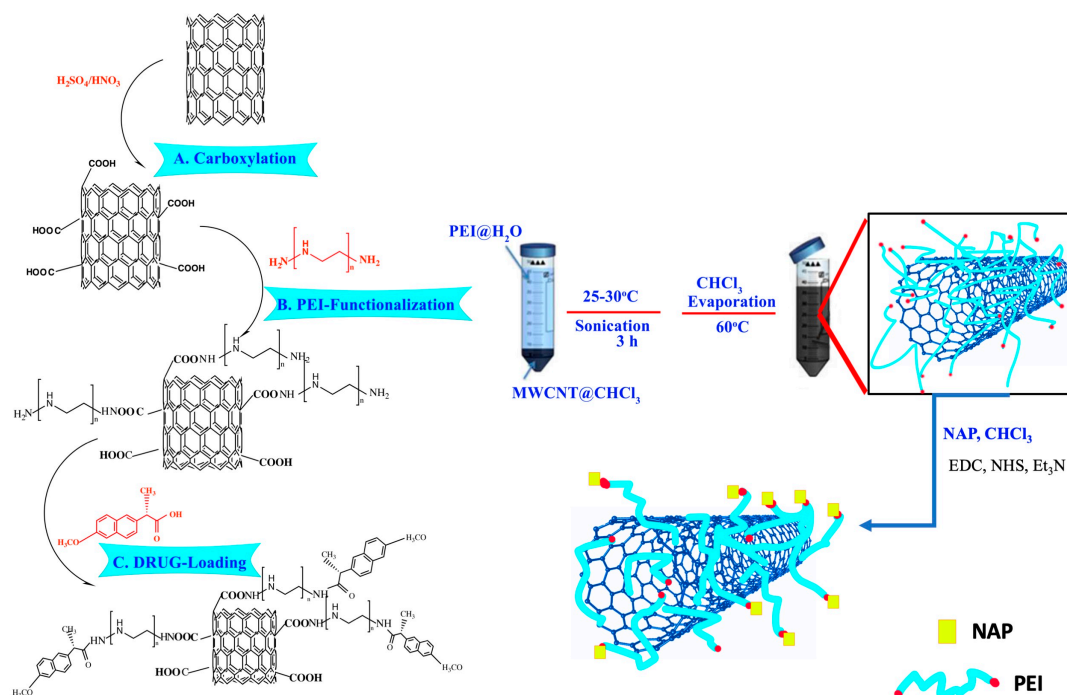


Figure 1. General synthetic strategy.

3.2. Magnetic Properties

The magnetic hysteresis curve at 4 K and in the field range from -6 to 6 Tesla and the ZFC-FC magnetic susceptibility measurements of the magnetic NL004 hybrid material are shown in Figure 2. In the inset of the same Figure is shown a magnification of the low field magnetization data in the form of M/M_s where the hysteresis loop of the hybrid material with a coercive field ca. 0.15 T is clearly resolved. The value of saturation magnetization, M_s , is 3.15 emu/g, due to the low percentage of ferromagnetic Fe/Ni catalyst residues (as it is already confirmed by manufacturer) while the value of M_r is close to 1.26 emu/gr. Having a value of M_r/M_s close to 0.5 (ca. 0.4), the magnetic nanoparticles are defined as a single-domain with a uniaxial anisotropy and randomly distributed easy axis at temperature well below the blocking temperature [52,53]. The temperature dependence of the magnetic susceptibility data of NL004, in the experimental mode of ZFC-FC with a very low external magnetic field (50 Oe), is also shown in Figure 2. The linear temperature dependence of the ZFC susceptibility data is related to the domain wall pinning processes [54] and the negative values at low temperatures are a direct consequence of the existence of magnetic interactions, possible crystal structure disorders and intrinsic negative spin polarization [55,56].

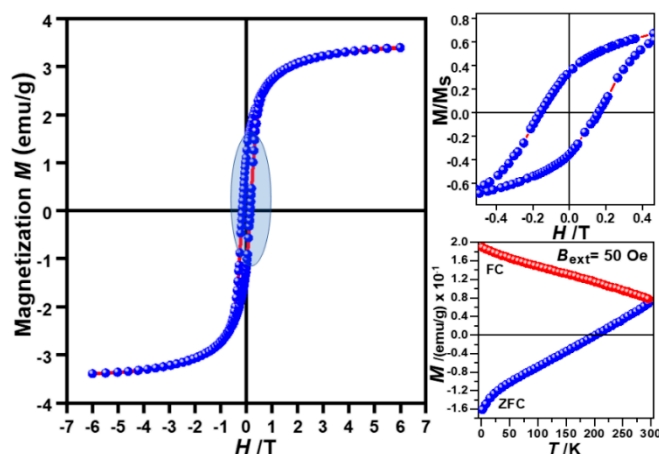


Figure 2. Field-dependent magnetization hysteresis curve of NL004 at 4 K. The blue-shaded area is shown for clarity reasons at the right part of the figure where the y -axis is given in the form of M/M_s with $M_s = 3.15$ emu/gr (saturation value of magnetization for NL004). At the right part is also shown the ZFC-FC temperature dependence of the DC susceptibility data of NL004 at external magnetic field of 50 Oe.

3.3. Raman Studies

In Figure 3 is shown the Raman spectra of raw and functionalized Mag-CNTs excited with the 785 nm laser line. The main features of these spectra are the so called: (a) D-band at ~ 1303 cm^{-1} ; (b) G-band at ~ 1580 cm^{-1} ; (c) D' at ~ 1601 cm^{-1} . The origin of the D- and D' bands is the double resonance Raman scattering process and are mainly disorder-induced features [57]. Their frequencies shift to higher values with the increase in the energy of the excitation laser while the intensity of the D' significantly decreases [58]. The pair of D and D' bands are usually attributed to the presence of amorphous or disordered carbon while the structural disorder is due to the finite or nanosized graphitic planes, defects on the nanotube walls and possibly other forms of carbon products. The G band originates from in-plane tangential stretching of the C–C bonds in the graphene sheets and it is doubly degenerate.

The profile characteristics of all Raman bands along with the intensity ratio I_D/I_G were deduced by Lorentzian fits on the Raman spectra (Figure 3) and summarized in Table 1. The high value of I_D/I_G for the pristine Mag-CNTs samples implies that pristine material is highly disordered or contains amorphous carbon (Table 1). The modification treatment of the pristine material either by COOH groups (NL002) or the PEI@NAP (NL004) results in an increase in the I_D/I_G ratio by about 21% and 16%, respectively. The position of the G band in the NL004 sample shifts to lower values (~ 4 cm^{-1}) with respect to the pristine CNTs suggesting that the treatment induces mechanical strain on the CNTs.

Table 1. The profile characteristics of D, G, D' Raman bands the intensity ratio (I_D/I_G).

	D (Pos, FWHM, A) *	G (Pos, FWHM, A)	D' (Pos, FWHM, A)	I_D/I_G
NL001	(1302.2, 71.0, 82.4)	(1579.5, 61.9, 38.7)	(1600.1, 33.1, 13.5)	2.13
NL002	(1307.3, 67.5, 152.9)	(1580.8, 56.7, 59.5)	(1606.5, 30.4, 25.8)	2.57
NL004	(1303.9, 69.0, 102.8)	(1575.7, 58.1, 41.8)	(1601.0, 29.2, 14.8)	2.46

* Pos = position in cm^{-1} , FWHM in cm^{-1} , A = area in 10^{-4} . All values based on averaged results from 5 spectra in each sample.

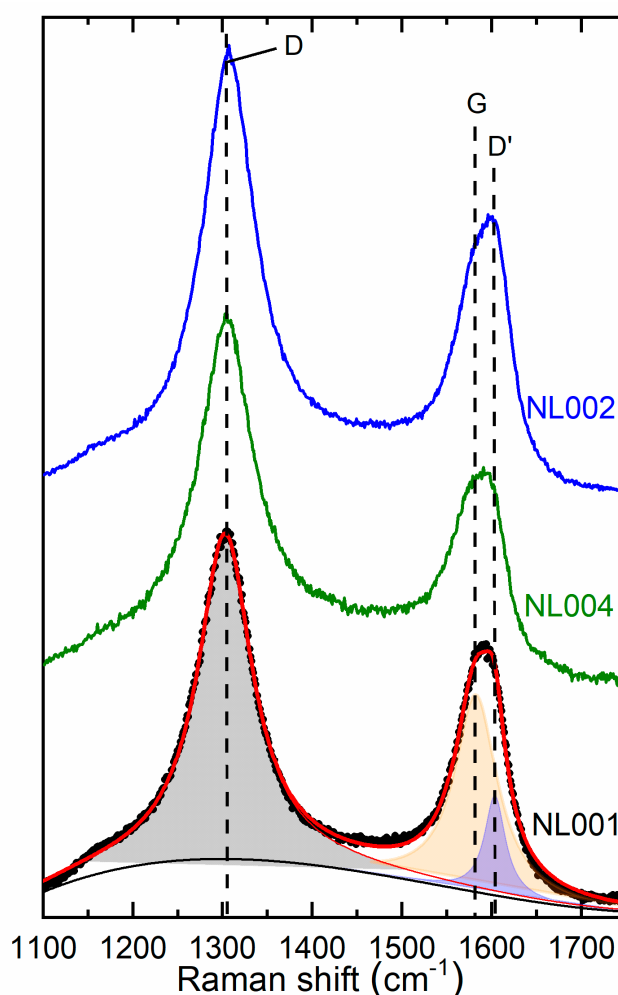


Figure 3. Indicative Raman spectra of the NL001, NL002, NL004 products where the characteristic D, G and D' Raman bands are shown.

3.4. Interaction with BSA

Serum albumin (SA) is among the most common proteins in blood plasma; SA has the role of transporting drugs, metal ions and/or complexes towards cells and tissues through the bloodstream. The intense fluorescence emission band of the BSA solution (3 μM) at 342 nm, when excited at 295 nm, is mainly attributed to the tryptophan residues found at positions 134 and 212 [44]. The inner-filter effect, as calculated with eq. S1, was negligible and slightly affected the measurements.

The addition of NL004 into the BSA solution resulted in a low-to-moderate quenching of $\sim 30\%$ of the initial fluorescence intensity of BSA fluorescence (Figure 4 and Figure S2). The observed intensity decrease in the fluorescence emission band at $\lambda = 342$ nm could be probably assigned to possible changes in the protein secondary structure leading to changes in the tryptophan environment of BSA stemming from the binding of NL004 to BSA [44].

The constants K_{SV} and k_{q} for NL004 were calculated by the Stern–Volmer quenching equation (eq. S2 and S3) and the corresponding Stern–Volmer plot (Figure S3) and are summarized in Table 2. More specifically, the derived k_{q} constant ($=2.05(\pm 0.10) \times 10^{12} \text{ M}^{-1}\text{s}^{-1}$) is much higher than the value of $2.0 \times 10^{10} \text{ M}^{-1}\text{s}^{-1}$ showing the existence of a static quenching mechanism [42]. The constant K of NL004, as calculated by the Scatchard equation (eq. S4) and the corresponding Scatchard plot (Figure S4), is relatively high ($=7.84(\pm 0.35) \times 10^4 \text{ M}^{-1}$) and within the range found for metal–NAP compounds [40,41,59,60]. Comparing the behavior towards BSA of NL004 containing functionalized

NAP with that of free NAP, we may conclude that functionalized NAP in NL004 presents higher quenching and binding constants than free NAP (Table 2).

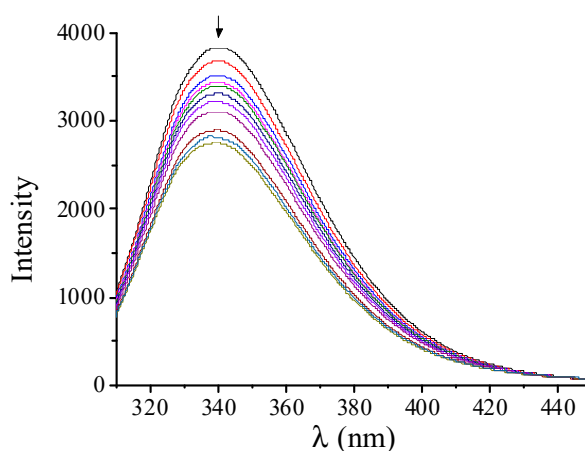


Figure 4. Fluorescence emission spectra ($\lambda_{\text{ex}} = 295 \text{ nm}$) of bovine serum albumin (BSA) ($3 \mu\text{M}$) in buffer solution (containing 15 mM trisodium citrate and 150 mM NaCl at pH 7.0) in the presence of increasing amounts of NL004 ($r = [\text{NL004}]/[\text{BSA}] = 0\text{--}6$). The arrow shows the changes upon increasing amounts of NL004.

Table 2. Comparison of the spectroscopic data (% of BSA fluorescence quenching), the quenching and the binding constants of NL004 and NAP for BSA (k_q , K).

Spectroscopic Data and Constants	NL004 ^a	NAP ^b
BSA fluorescence quenching ($\Delta I/I_0$, %)	29.1	23.0
K_{SV} (M^{-1})	$2.05(\pm 0.10) \times 10^4$	$1.18(\pm 0.06) \times 10^4$
k_q ($\text{M}^{-1}\text{s}^{-1}$)	$2.05(\pm 0.10) \times 10^{12}$	$1.18(\pm 0.06) \times 10^{12}$
K (M^{-1})	$7.84(\pm 0.35) \times 10^4$	$5.35(\pm 0.42) \times 10^3$
N	0.40	2.14

^a this work; ^b Dimiza, F.; Perdih, F.; Tangoulis, V.; Turel, I.; Kessissoglou D.P.; Psomas, G. Interaction of copper(II) with the non-steroidal anti-inflammatory drugs naproxen and diclofenac: synthesis, structure, DNA- and albumin-binding. *J. Inorg. Biochem.*, **2011**, *105*, 476–489.

In total, the K constant of NL004 to BSA seems high enough to suggest its attachment to BSA in order to become transported. It is also much lower than the value of 10^{15} M^{-1} (= the binding constant of avidin with diverse compounds; these constitute the strongest known non-covalent binding); therefore, the binding of NL004 to BSA seems reversible, proposing the releasing ability upon arrival at potential biological targets [61].

3.5. Interaction with DNA

The interaction of double-stranded DNA with diverse compounds may take place via either covalent (replacement of a labile ligand of the complex by a nitrogenous DNA base, as in the case of *cisplatin*) or non-covalent fashion (intercalation, electrostatic interactions and groove-binding) [62]. Furthermore, the interaction of compounds containing NSAIDs, such as NAP with double-stranded DNA, may be connected to potential anticancer, antioxidant and/or anti-inflammatory activities. Therefore, the *in vitro* DNA-binding of NL004 was studied by UV-vis spectroscopy and viscosity measurements and via the ability to displace the typical DNA-intercalator EB, and was compared to the behavior of free NAP which has been already reported [40,41].

UV-vis spectroscopy is usually used to study the DNA-binding mode and to calculate the DNA-binding strength. Any changes of the DNA UV-band or the intraligand transition bands of the compounds may be due to their interaction and may reveal their possible mode. The UV-vis spectra

of a CT DNA solution (0.18 mM) were recorded in the presence of increasing amounts of NL004; the DNA UV-band at 258 nm exhibited hypochromism (Figure 5A) suggesting the interaction of NL004 with CT DNA [63]. In the UV-vis spectra of NL004, diverse bands were observed with most of them being attributed to the nanotube and band located at 324 nm, which are attributed to NAP (Figure 5B). Upon addition of CT DNA, all these UV-bands of NL004 exhibited considerable hypochromism (up to ~40%) and were followed by a slight red-shift or were eliminated (Table 3).

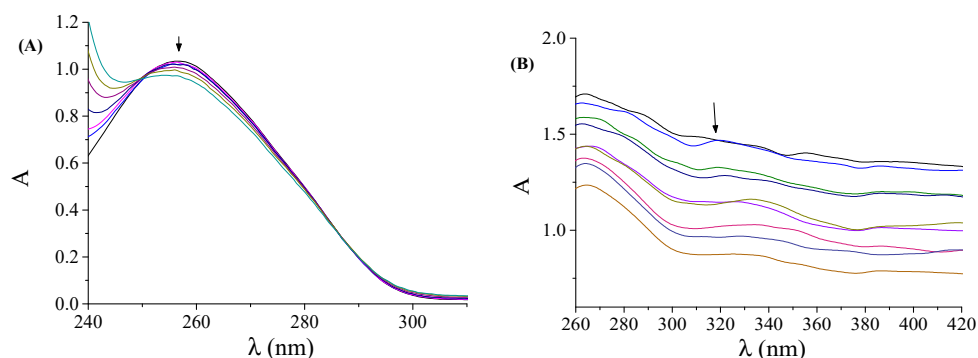


Figure 5. (A) UV-vis spectra of calf-thymus (CT) DNA (0.18 mM) in buffer solution (150 mM NaCl and 15 mM trisodium citrate at pH 7.0) in the absence or presence of increasing amounts of NL004 ($r = [\text{NL004}]/[\text{DNA}] = 0-0.5$). The arrow shows the changes upon increasing amounts of NL004. (B) UV-vis spectra of NL004 in DMSO in the presence of increasing amounts of CT DNA ($r' = [\text{DNA}]/[\text{NL004}] = 0-0.5$). The arrow shows the changes upon increasing amounts of CT DNA.

Table 3. Comparison of the spectroscopic data (changes of the UV-band, % of ethidium bromide (EB)-DNA fluorescence quenching), the quenching and the binding constants of NL004 and free NAP for CT DNA (K_b) and competitive studies with EB (K_{sv} , k_q).

Spectroscopic Data and Constants	NL004 ^a	NAP ^b
$\lambda(\text{nm}) (\Delta A/A_0(\%), \Delta\lambda(\text{nm}))^c$	265 (−27, 0); 311 (−40, elm ^d); 324 (−39, +6); 355 (−40, elm)	325(+22, +2)
$K_b (\text{M}^{-1})$	$8.66(\pm 0.07) \times 10^4$	$2.67(\pm 0.22) \times 10^4$
EB-DNA fluorescence quenching ($\Delta I/I_0, \%$)	50.7	82.0
$K_{sv} (\text{M}^{-1})$	$3.37(\pm 0.10) \times 10^4$	$1.47(\pm 0.04) \times 10^5$
$k_q (\text{M}^{-1}\text{s}^{-1})$	$1.47(\pm 0.04) \times 10^{12}$	$6.39(\pm 0.17) \times 10^{12}$

^a this work; ^b Dimiza, F.; Perdih, F.; Tangoulis, V.; Turel, I.; Kessissoglou D.P.; Psomas, G. Interaction of copper(II) with the non-steroidal anti-inflammatory drugs naproxen and diclofenac: synthesis, structure, DNA- and albumin-binding. *J. Inorg. Biochem.*, **2011**, *105*, 476–489. ^c UV-band (λ in nm) (percentage of the hyper-/hypochromism ($\Delta A/A_0, \%$), blue-/red-shift of the λ_{max} ($\Delta\lambda, \text{nm}$)); ^d elm = eliminated.

The DNA-binding constant K_b of NL004 was calculated by the Wolfe–Shimer equation (eq. S4) [44] and the corresponding plot $[\text{DNA}]/(\varepsilon_A - \varepsilon_f)$ versus CT DNA (Figure S5). The K_b constant of NL004 ($= 8.66(\pm 0.07) \times 10^4 \text{ M}^{-1}$) is approximately three times higher than that of free NAP (Table 3) suggesting that the functionalization of NAP in NL004 may result in an enhanced affinity for CT DNA. In addition, the K_b of NL004 is in the range reported for metal–NAP complexes [36,51,52] and is close to the K_b constant of the classical intercalator ethidium bromide (EB) ($K_b = 1.23(\pm 0.07) \times 10^5 \text{ M}^{-1}$), as calculated by Dimitrakopoulou et al. [64].

The features from the UV-vis spectroscopic titrations may suggest the binding of functionalized NAP to CT DNA; the observed hypochromism may reveal the possibility of an intercalative interaction mode, although significant steric hindrance may exclude it. Therefore, in order to conclude the DNA-binding fashion of NL004, DNA-viscosity measurements and EB-competitive studies were carried out [63,65].

The study of DNA-viscosity is an essential technique in order to clarify/verify the DNA-interaction mode of a compound, because of the sensitiveness of the DNA-viscosity to relative DNA-length changes [66]. As it is known, in the case of classic intercalation of a compound in-between the DNA base pairs, the DNA base pairs' separation distance at intercalation sites, and consequently the relative DNA-length, will increase so that the bound compound is hosted inducing thus an increase in DNA-viscosity. When non-classical intercalation (including groove-binding and electrostatic interaction) occurs, the relative DNA-length remains the same or decreases slightly because of the DNA-helix bending; thus, the relative DNA-viscosity will remain stable or will present a slight increase [66]. The viscosity of the CT DNA solution (0.1 mM) was measured by adding increasing amounts of NL004 and a slight decrease in the relative DNA-viscosity was observed (Figure 6). Therefore, the changes of the relative DNA-viscosity may suggest the absence of a classical intercalation between NL004 and CT DNA; taking also into consideration the steric hindrance induced by the nanotube, we may suggest that the interaction of functionalized NAP in NL004 probably takes place via the external interaction mode.

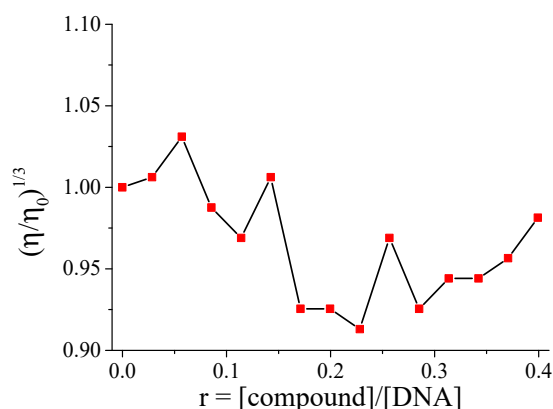


Figure 6. Relative viscosity $(\eta/\eta_0)^{1/3}$ of CT DNA (0.1 mM) in buffer solution (150 mM NaCl and 15 mM trisodium citrate at pH 7.0) in the presence of NL004 at increasing amounts ($r = [\text{NL004}]/[\text{DNA}]$).

EB is a typical indicator of intercalation [67]. The DNA-intercalation of EB occurs via the insertion of the planar EB-phenanthridine ring in-between adjacent DNA bases resulting in the formation of an EB-DNA conjugate which exhibits an intense fluorescence emission band at 592 nm. The addition of intercalating compounds into the EB-DNA solution will obviously result in a significant quenching of the EB-DNA emission band because of the displacement of EB in the EB-DNA conjugate by the inserting compounds which can bind to DNA equally or even more strongly than EB. The fluorescence emission spectra of an EB-DNA solution ($[\text{EB}] = 20 \mu\text{M}$, $[\text{DNA}] = 26 \mu\text{M}$) were recorded in the absence and presence of increasing amounts of NL004 (Figure 7). The addition of NL004 resulted in a moderate decrease (up to 50%, Figure S6) in the intensity of the emission band at 592 nm. The observed fluorescence quenching (Table 3) is rather moderate and may indicate a relatively low competition of the NL044 with EB in its binding to DNA, although the DNA-binding constant of NL044 is close to that of EB. Consequently, we may suggest that the intercalating ability of NL044 is rather low [52,53] and the intercalation between NL004 and CT DNA should not be expected, in accordance to DNA-viscosity measurements. The linear Stern-Volmer equation (eq. S2) and the corresponding Stern-Volmer plot of EB-DNA ($R = 0.99$, Figure S7) proved that the EB-DNA fluorescence emission quenching might be a result of the partial displacement of EB in EB-DNA by NL004. The calculated Stern-Volmer constant (K_{sv}) and quenching constant (k_q , as calculated from eq. S3 for fluorescence lifetime of the EB-DNA system, $\tau_0 = 23 \text{ ns}$ [42]) of NL004 (Table 3) are significantly lower than those of free NAP, thus showing a lower ability to displace EB.

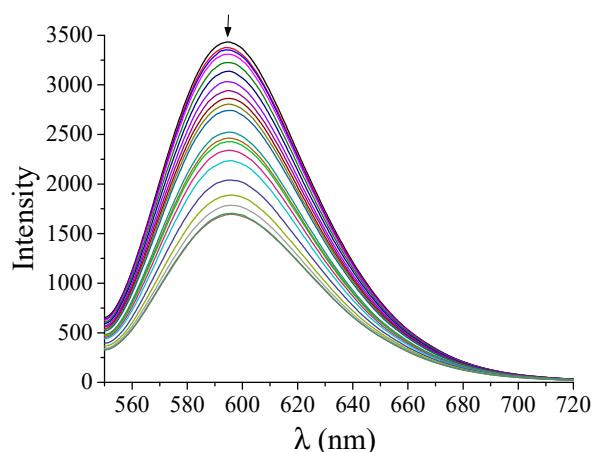


Figure 7. Fluorescence emission spectra ($\lambda_{\text{exc}} = 540 \text{ nm}$) for EB-DNA ($[\text{EB}] = 20 \mu\text{M}$, $[\text{DNA}] = 26 \mu\text{M}$) in buffer solution in the absence and presence of increasing amounts of NL004 (up to the value of $r = [\text{NL004}]/[\text{DNA}] = 0.45$). The arrow shows the changes of intensity upon increasing amounts of NL004.

3.6. Drug-Release Studies

The emission spectra of free NAP solution and the suspension of NL004 are presented in Figure 8. No emission was detected for the raw carboxylated Mag-CNTs (NL002) and the PEI-functionalized Mag-CNTs (NL003). Comparison between the spectra of the free NAP solution ($\lambda_{\text{max,em}} = 357 \text{ nm}$) and NL004 ($\lambda_{\text{max,em}} = 405 \text{ nm}$) reveals a significant broadening and a red-shift in the maximum emission wavelength for the latter one. Both these features can be attributed to changes in the chemical environment surrounding the drug molecule due to the location of this drug in NL004 [68,69]. These findings confirm a successful incorporation of NAP in NL004. The characteristic shoulder observed at the spectrum of the suspension at 357 nm comes from free NAP.

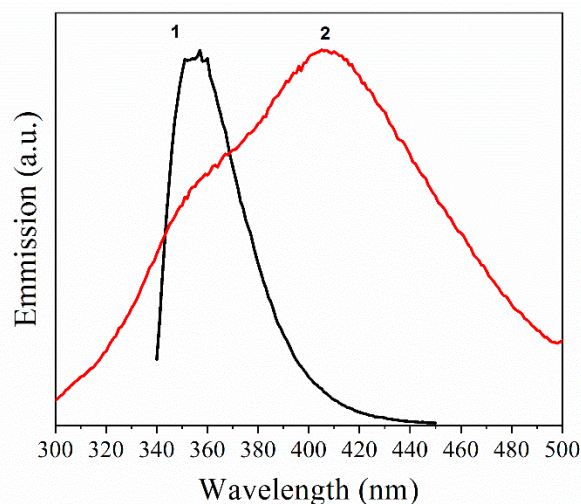


Figure 8. Normalized fluorescence spectra of (1) Naproxen (NAP) solution; (2) suspension of NL004, excitation wavelength (259 nm).

It is well known that acidic conditions are typical of inflamed tissues. In order to check if we have a pH-sensitive targeted drug-delivery, three representative pH values (acidic, neutral and basic) were chosen [68]. The release of the drug from NL004 was tested at pH 4.1, 6.8 and 10.1. Figure 9 summarizes the results. At pH 4.1, the release profile indicates a rapid release up to a maximum of 42% NAP within the first 50 min. This corresponds to 0.38 mg of released NAP. Moreover, the release

experiment conducted at pH 6.8 and 10.1 indicated a much lower percentage of NAP release (19% and 16%, respectively).

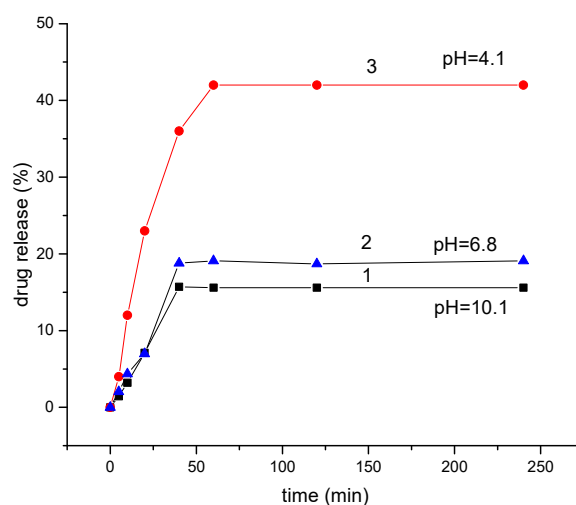


Figure 9. Release of NAP from the NL004 at pH 10.1 (1), 6.8 (2) and 4.1 (3) assessed by fluorescence measurements under excitation at 259 nm.

4. Conclusions

A facile and effective way for the attachment of Naproxen (NAP), a carboxylate NSAID, on the surface of PEI-functionalized carboxylated Mag-CNTs was presented based on the indirect coupling of NAP through the amino groups of the intermediate linker PEI. The interaction of the designed nanocarrier with BSA was studied in vitro by fluorescence emission spectroscopy while its in vitro interaction to bind to CT DNA was monitored by UV-vis spectroscopy and viscosity measurements and via competitive studies with ethidium bromide. The calculated binding constants were compared to those of free NAP revealing a higher binding affinity for BSA and CT DNA. Finally, drug-release studies were performed, revealing that the electrostatic linkage ensures an effective release of the drug in the acidic pH typical of inflamed cells, while maintaining the MWNT-drug conjugates stable at the typical bloodstream.

Supplementary Materials: The following are available online at <http://www.mdpi.com/2311-5629/6/4/62/s1>, Figure S1: FT-IR spectra. Figures S2–S7: The Stern–Volmer and Scatchard graphs from interaction with serum albumins and interaction with CT-DNA.

Author Contributions: V.T. contributed in the project administration, conceptualization, visualization, and writing-reviewing of original draft. N.L. (Nikolia Lalioti) contributed in the methodology, supervision of the synthetic methodology and revised the paper. J.P. contributed in Raman measurements and revised the paper. N.L. (Nathan Langford) contributed in the synthetic methodology. E.V.-J. contributed in resources, Project administration funding and revised the paper. C.K. contributed in the biological studies. G.P. contributed in the methodology and supervision of the biological studies and revised the paper. V.B. contributed in photoluminescence and drug release measurements and revised the paper. All authors have read and agreed to the published version of the manuscript.

Funding: This research has been partially performed within the framework of project NANOGENTOOLS, under the Marie Skłodowska-Curie grant agreement No 691095. The author CK acknowledges the financial support via a scholarship from the General Secretariat for Research and Technology (GSRT) and Hellenic Foundation for Research and Innovation (HFRI), Greek Ministry of Education, Research and Religion.

Conflicts of Interest: The authors declare no conflict of interest.

References

1. Dalton, A.B.; Collins, S.; Munoz, E.; Razal, J.M.; Ebron, V.H.; Ferraris, J.P.; Coleman, J.N.; Kim, B.G.; Baughman, R.H. Super-tough carbon-nanotube fibres. *Nature* **2003**, *423*, 703. [[CrossRef](#)]

2. Hibino, N.; Suzuki, S.; Wakahara, H.; Kobayashi, Y.; Sato, T.; Maki, H. Short-Wavelength Electroluminescence from Single-Walled Carbon Nanotubes with High Bias Voltage. *ACS Nano* **2011**, *5*, 1215–1222. [[CrossRef](#)] [[PubMed](#)]
3. Luo, H.; Shi, Z.; Li, N.; Gu, Z.; Zhuang, Q. Investigation of the Electrochemical and Electrocatalytic Behavior of Single-Wall Carbon Nanotube Film on a Glassy Carbon Electrode. *Anal. Chem.* **2001**, *73*, 915–920. [[CrossRef](#)] [[PubMed](#)]
4. Shim, M.; Kam, N.W.S.; Chen, R.J.; Li, Y.M.; Dai, H.J. Functionalization of Carbon Nanotubes for Biocompatibility and Biomolecular Recognition. *Nano Lett.* **2002**, *2*, 285–288. [[CrossRef](#)]
5. Chen, J.; Chen, S.; Zhao, X.; Kuznetsova, L.V.; Wong, S.S.; Ojima, I. Functionalized Single-Walled Carbon Nanotubes as Rationally Designed Vehicles for Tumor-Targeted Drug Delivery. *J. Am. Chem. Soc.* **2008**, *130*, 16778–16785. [[CrossRef](#)] [[PubMed](#)]
6. Wei, G.; Zhang, J.; Xie, L.; Jandt, K.D. Biomimetic growth of hydroxyapatite on super water-soluble carbon nanotube-protein hybrid nanofibers. *Carbon* **2011**, *49*, 2216–2226. [[CrossRef](#)]
7. Tasis, D.; Tagmatarchis, N.; Bianco, A.; Prato, M. Chemistry of Carbon Nanotubes. *Chem. Rev.* **2006**, *106*, 1105–1136. [[CrossRef](#)]
8. Wei, G.; Pan, C.; Reichert, J.; Jandt, K.D. Controlled assembly of protein-protected gold nanoparticles on noncovalent functionalized carbon nanotubes. *Carbon* **2010**, *48*, 645–653. [[CrossRef](#)]
9. Wei, G.; Xu, F.; Li, Z.; Jandt, K.D. Protein-Promoted Synthesis of Pt Nanoparticles on Carbon Nanotubes for Electrocatalytic Nanohybrids with Enhanced Glucose Sensing. *J. Phys. Chem. C* **2011**, *115*, 11453–11460. [[CrossRef](#)]
10. Foillard, S.; Zuber, G.; Doris, E. Polyethylenimine–carbon nanotube nanohybrids for siRNA-mediated gene silencing at cellular level. *Nanoscale* **2011**, *3*, 1461–1464. [[CrossRef](#)]
11. McNicholas, T.P.; Yum, K.; Ahn, J.H.; Mu, B.; Plettenburg, O.; Gooderman, A.; Natesan, S.; Strano, M.S. Structure and function of glucose binding protein-single walled carbon nanotube complexes. *Small* **2012**, *8*, 3510–3516. [[CrossRef](#)] [[PubMed](#)]
12. Maeda, H. The enhanced permeability and retention (EPR) effect in tumor vasculature: The key role of tumor-selective macromolecular drug targeting. *Adv. Enzyme Regul.* **2001**, *41*, 189–207. [[CrossRef](#)]
13. Iyer, A.K.; Khaled, G.; Fang, J.; Maeda, H. Exploiting the enhanced permeability and retention effect for tumor targeting. *Drug Discov. Today* **2006**, *11*, 812–818. [[CrossRef](#)]
14. Kostarelos, K.; Lacerda, L.; Pastorin, G.; Wu, W.; Wieckowski, S.; Luangsivilay, J.; Godefroy, S.; Pantarotto, D.; Briand, J.P.; Muller, S.; et al. Cellular uptake of functionalized carbon nanotubes is independent of functional group and cell type. *Nat. Nanotechnol.* **2007**, *2*, 108–113. [[CrossRef](#)] [[PubMed](#)]
15. Lacerda, L.; Russier, J.; Pastorin, G.; Herrero, M.A.; Venturelli, E.; Dumortier, H.; Al-Jamal, K.T.; Prato, M.; Kostarelos, K.; Bianco, A. Translocation mechanisms of chemically functionalized carbon nanotubes across plasma membranes. *Biomaterials* **2012**, *33*, 3334–3343. [[CrossRef](#)]
16. Boncel, S.; Zajac, P.; Koziol, K.K. Liberation of drugs from multi-wall carbon nanotube carriers. *J. Control Release* **2013**, *169*, 126–140. [[CrossRef](#)]
17. Karousis, N.; Tagmatarchis, N.; Tasis, D. Current Progress on the Chemical Modification of Carbon Nanotubes. *Chem. Rev.* **2010**, *110*, 5366–5397. [[CrossRef](#)]
18. Wu, H.C.; Chang, X.; Liu, L.; Zhao, F.; Zhao, Y. Chemistry of carbon nanotubes in biomedical applications. *J. Mater. Chem.* **2010**, *20*, 1036–1052. [[CrossRef](#)]
19. Singh, P.S.; Campidelli, S.; Giordani, S.; Bonifazi, D.; Bianco, A.; Prato, M. Organic functionalisation and characterisation of single-walled carbon nanotubes. *Chem. Soc. Rev.* **2009**, *38*, 2214–2230. [[CrossRef](#)]
20. Peng, X.; Wong, S.S. Functional Covalent Chemistry of Carbon Nanotube Surfaces. *Adv. Mater.* **2009**, *21*, 625–642. [[CrossRef](#)]
21. Lee, Y.; Geckeler, K.E. Carbon Nanotubes in the Biological Interphase: The Relevance of Noncovalence. *Adv. Mater.* **2010**, *22*, 4076–4083. [[CrossRef](#)]
22. Zhao, Y.L.; Stoddart, J.F. Noncovalent Functionalization of Single-Walled Carbon Nanotubes. *Acc. Chem. Res.* **2009**, *42*, 1161–1171. [[CrossRef](#)]
23. Bianco, A.; Kostarelos, K.; Prato, M. Making carbon nanotubes biocompatible and biodegradable. *Chem. Commun.* **2011**, *47*, 10182–10188. [[CrossRef](#)]
24. Fabbro, C.; Ali-Boucetta, H.; Ros, T.D.; Kostarelos, K.; Bianco, A.; Prato, M. Targeting carbon nanotubes against cancer. *Chem. Commun.* **2012**, *48*, 3911–3926. [[CrossRef](#)]

25. Hong, H.; Gao, T.; Cai, W. Molecular Imaging with Single-Walled Carbon Nanotubes. *Nano Today* **2009**, *4*, 252–261. [[CrossRef](#)]
26. Liu, Z.; Yang, K.; Lee, S.T. Single-walled carbon nanotubes in biomedical imaging. *J. Mater. Chem.* **2011**, *21*, 586–598. [[CrossRef](#)]
27. Kuznik, N.; Tomczyk, M.M. Multiwalled carbon nanotube hybrids as MRI contrast agents. *Beilstein J. Nanotechnol.* **2016**, *7*, 1086–1103. [[CrossRef](#)]
28. Vittorio, O.; Duce, S.L.; Pietrabissa, A.; Cuschieri, A. Multiwall carbon nanotubes as MRI contrast agents for tracking stem cells. *Nanotechnology* **2011**, *22*, 095706. [[CrossRef](#)]
29. Masotti, A.; Caporali, A. Preparation of Magnetic Carbon Nanotubes (Mag-CNTs) for Biomedical and Biotechnological Applications. *Int. J. Mol. Sci.* **2013**, *14*, 24619–24642. [[CrossRef](#)]
30. Battigelli, A.; Ménard-Moyon, C.; Ros, T.D.; Prato, M.; Bianco, A. Endowing carbon nanotubes with biological and biomedical properties by chemical modifications. *Adv. Drug Deliv. Rev.* **2013**, *65*, 1899–1920. [[CrossRef](#)]
31. Zeinabad, H.A.; Zarrabian, A.; Saboury, A.A.; Alizadeh, A.M.; Falahati, M. Interaction of single and multiwall carbon nanotubes with the biological systems: Tau protein and PC12 cells as targets. *Sci. Rep.* **2016**, *6*, 26508. [[CrossRef](#)]
32. Meek, L.I.; van der Laar, A.F.J.M.; Vonkeman, E.H. Non Steroidal Anti-Inflammatory Drugs: An overview of Cardiovascular Risks. *Pharmaceuticals* **2010**, *3*, 2146–2162. [[CrossRef](#)]
33. Weder, J.E.; Dillon, C.T.; Hambley, T.W.; Kennedy, B.J.; Lay, P.A.; Biffin, J.R.; Regtop, H.L.; Davies, N.M. Copper Complexes of Non-steroidal Anti-inflammatory Drugs: An Opportunity yet to be Realized. *Coord. Chem. Rev.* **2002**, *232*, 95–126. [[CrossRef](#)]
34. Psomas, G.; Kessissoglou, D.P. Quinolones and Non-Steroidal Antiinflammatory Drugs Interacting with Copper(II), Nickel(II), Cobalt(II) and Zinc(II): Structural Features, Biological Evaluation and Perspectives. *Dalton Trans.* **2013**, *42*, 6252–6276. [[CrossRef](#)]
35. Banti, C.N.; Hadjikakou, S.K. Non-Steroidal Anti-Inflammatory Drugs (NSAIDs) in Metal Complexes and Their Effect at the Cellular Level. *Eur. J. Inorg. Chem.* **2016**, 3048–3071. [[CrossRef](#)]
36. Psomas, G. Copper(II) and zinc(II) coordination compounds of non-steroidal anti-inflammatory drugs: Structural features and antioxidant activity. *Coord. Chem. Rev.* **2020**, *412*, 213259. [[CrossRef](#)]
37. Habibizadeh, M.; Rostamizadeh, K.; Dalali, N.; Ramazani, A. Preparation and characterization of PEGylated multiwall carbon nanotubes as covalently conjugated and non-covalent drug carrier: A comparative study. *Mat. Sci. Eng. C* **2017**, *74*, 1–9. [[CrossRef](#)]
38. Marmur, J. A procedure for the isolation of deoxyribonucleic acid from micro-organisms. *J. Mol. Biol.* **1961**, *3*, 208–218. [[CrossRef](#)]
39. Reichmann, M.F.; Rice, S.A.; Thomas, C.A.; Doty, P. A Further Examination of the Molecular Weight and Size of Desoxypentose Nucleic Acid. *J. Am. Chem. Soc.* **1954**, *76*, 3047–3053. [[CrossRef](#)]
40. Dimiza, F.; Perdih, F.; Tangoulis, V.; Turel, I.; Kessissoglou, D.P.; Psomas, G. Interaction of copper(II) with the non-steroidal anti-inflammatory drugs naproxen and diclofenac: Synthesis, structure, DNA- and albumin-binding. *J. Inorg. Biochem.* **2011**, *105*, 476–489. [[CrossRef](#)]
41. Dimiza, F.; Raptopoulou, C.P.; Psycharis, V.; Papadopoulos, A.N.; Psomas, G. Manganese(II) complexes with the non-steroidal anti-inflammatory drugs naproxen and mefenamic acid. Synthesis, structure, antioxidant capacity, interaction with albumins and DNA. *N. J. Chem.* **2018**, *42*, 16666–16681. [[CrossRef](#)]
42. Lakowicz, J.R. *Principles of Fluorescence Spectroscopy*, 3rd ed.; Plenum Press: New York, NY, USA, 2006.
43. Stella, L.; Capodilupo, A.L.; Bietti, M. A reassessment of the association between azulene and [60]fullerene. Possible pitfalls in the determination of binding constants through fluorescence spectroscopy. *Chem. Commun.* **2008**, 4744–4746. [[CrossRef](#)] [[PubMed](#)]
44. Wang, Y.; Zhang, H.; Zhang, G.; Tao, W.; Tang, S. Interaction of the flavonoid hesperidin with bovine serum albumin: A fluorescence quenching study. *J. Lumin.* **2007**, *126*, 211–218. [[CrossRef](#)]
45. Wolfe, A.; Shimer, G.; Meehan, T. Polycyclic aromatic hydrocarbons physically intercalate into duplex regions of denatured DNA. *Biochemistry* **1987**, *26*, 6392–6396. [[CrossRef](#)]
46. Zhao, G.; Lin, H.; Zhu, S.; Sun, H.; Chen, Y. Dinuclear palladium(II) complexes containing two monofunctional [Pd(en)(pyridine)Cl]⁺ units bridged by Se or S. Synthesis, characterization, cytotoxicity and kinetic studies of DNA-binding. *J. Inorg. Biochem.* **1998**, *70*, 219–226. [[CrossRef](#)]
47. Heller, D.P.; Greenstock, C.L. Fluorescence lifetime analysis of DNA intercalated ethidium bromide and quenching by free dye. *Biophys. Chem.* **1994**, *50*, 305–312. [[CrossRef](#)]

48. Liu, Y.; Wu, D.C.; Zhang, W.D.; Jiang, X.; He, C.B.; Chung, T.S.; Goh, S.H.; Leong, K.W. Polyethylenimine-grafted multiwalled carbon nanotubes for secure noncovalent immobilization and efficient delivery of DNA. *Angew. Chem. Int. Ed. Engl.* **2005**, *44*, 4782–4785. [[CrossRef](#)]
49. Wang, L.; Shi, J.; Zhang, H.; Li, H.; Gao, Y.; Wang, Z.; Wang, H.; Li, L.; Zhang, C.; Chen, C.; et al. Synergistic anticancer effect of RNAi and photothermal therapy mediated by functionalized single-walled carbon nanotubes. *Biomaterials* **2013**, *34*, 262–274. [[CrossRef](#)]
50. Huang, Y.P.; Lin, I.J.; Chen, C.C.; Hsu, Y.C.; Chang, C.C.; Lee, M.J. Delivery of small interfering RNAs in human cervical cancer cells by polyethylenimine-functionalized carbon nanotubes. *Nanoscale Res. Lett.* **2013**, *8*, 267–278. [[CrossRef](#)]
51. Georgiadou, V.; Makris, G.; Papagiannopoulou, D.; Vourlias, G.; Dendrinou-Samara, C. Octadecylamine-Mediated Versatile Coating of CoFe₂O₄ NPs for the Sustained Release of Anti-inflammatory Drug Naproxen and in vivo Target Selectivity. *Appl. Mater. Interfaces* **2016**, *8*, 9345–9360. [[CrossRef](#)]
52. Zhang, X.X.; Wen, G.H.; Huang, S.; Dai, L.; Gao, R.; Wang, Z.L. Magnetic properties of Fe nanoparticles trapped at the tips of the aligned carbon nanotubes. *J. Magn. Magn. Mater.* **2001**, *231*, L9–L12. [[CrossRef](#)]
53. Gozzi, D.; Latini, A.; Capannelli, G.; Canepa, F.; Napoletano, M.; Cimberle, M.R.; Tropeano, M. Synthesis and magnetic characterization of Ni nanoparticles and Ni nanoparticles in multiwalled carbon nanotubes. *J. Alloys Comp.* **2006**, *419*, 32–39. [[CrossRef](#)]
54. Zhang, X.X.; Hernández, J.M.; Tejada, J.; Solé, R.; Ruiz, X. Magnetic properties and domain-wall motion in single-crystal BaFe_{10.2}Sn_{0.74}Co_{0.66}O₁₉. *Phys. Rev. B* **2006**, *53*, 3336–3340. [[CrossRef](#)]
55. Kumar, A.; Yusuf, S.M. The phenomenon of negative magnetization and its implications. *Phys. Rep.* **2015**, *556*, 1–34. [[CrossRef](#)]
56. Sarkar, B.; Dalal, B.; De, S.K. Temperature induced magnetization reversal in SrRuO₃. *Appl. Phys. Lett.* **2013**, *103*, 252403. [[CrossRef](#)]
57. Dresselhaus, M.S.; Dresselhaus, G.; Saito, R.; Jorio, A. Raman spectroscopy of carbon nanotubes. *Phys. Rep.* **2005**, *409*, 47–99. [[CrossRef](#)]
58. Pimenta, M.A.; Dresselhaus, G.; Dresselhaus, M.S.; Cañado, L.G.; Jorio, A.; Saito, R. Studying disorder in graphite-based systems by Raman spectroscopy. *Phys. Chem. Chem. Phys.* **2007**, *9*, 1276–1291. [[CrossRef](#)]
59. Dimiza, F.; Papadopoulos, A.N.; Tangoulis, V.; Psycharis, V.; Raptopoulou, C.P.; Kessissoglou, D.P.; Psomas, G. Biological evaluation of cobalt(II) complexes with non-steroidal anti-inflammatory drug naproxen. *J. Inorg. Biochem.* **2012**, *107*, 54–64. [[CrossRef](#)]
60. Totta, X.; Hatzidimitriou, A.G.; Papadopoulos, A.N.; Psomas, G. Nickel(II)-naproxen Mixed-Ligand Complexes: Synthesis, Structure, Antioxidant Activity and Interaction with Albumins and Calf-Thymus DNA. *New J. Chem.* **2017**, *41*, 4478–4492. [[CrossRef](#)]
61. Rajendiran, V.; Karthik, R.; Palaniandavar, M.; Stoeckli-Evans, H.; Periasamy, V.S.; Akbarsha, M.A.; Srinag, B.S.; Krishnamurthy, H. Mixed-Ligand Copper(II)-phenolate Complexes: Effect of Coligand on Enhanced DNA and Protein Binding, DNA Cleavage, and Anticancer Activity. *Inorg. Chem.* **2007**, *46*, 8208–8221. [[CrossRef](#)]
62. Roy, S.; Banerjee, R.; Sarkar, M. Direct binding of Cu(II)-complexes of oxicam NSAIDs with DNA backbone. *J. Inorg. Biochem.* **2006**, *100*, 1320–1331. [[CrossRef](#)] [[PubMed](#)]
63. Pyle, A.M.; Rehmann, J.P.; Meshoyrer, R.; Kumar, C.V.; Turro, N.J.; Barton, J.K. Mixed-ligand complexes of ruthenium(II): Factors governing binding to DNA. *J. Am. Chem. Soc.* **1989**, *111*, 3051–3058. [[CrossRef](#)]
64. Dimitrakopoulou, A.; Dendrinou-Samara, C.; Pantazaki, A.A.; Alexiou, M.; Nordlander, E.; Kessissoglou, D.P. Synthesis, structure and interactions with DNA of novel tetranuclear, [Mn₄(II/II/II/IV)] mixed valence complexes. *J. Inorg. Biochem.* **2008**, *102*, 618–628. [[CrossRef](#)] [[PubMed](#)]
65. Pratviel, G.; Bernadou, J.; Meunier, B. DNA and RNA Cleavage by Metal Complexes. *Adv. Inorg. Chem.* **1998**, *45*, 251–262.
66. Garcia-Gimenez, J.L.; Gonzalez-Alvarez, M.; Liu-Gonzalez, M.; Macias, B.; Borrás, J.; Alzuet, G. Toward the development of metal-based synthetic nucleases: DNA binding and oxidative DNA cleavage of a mixed copper(II) complex with N-(9H-purin-6-yl)benzenesulfonamide and 1,10-phenanthroline. Antitumor activity in human Caco-2 cells and Jurkat T lymphocytes. Evaluation of p53 and Bcl-2 proteins in the apoptotic mechanism. *J. Inorg. Biochem.* **2009**, *103*, 923–934.
67. Wilson, W.D.; Ratmeyer, L.; Zhao, M.; Streckowski, L.; Boykin, D. The search for structure-specific nucleic acid-interactive drugs: Effects of compound structure on RNA versus DNA interaction strength. *Biochemistry* **1993**, *32*, 4098–4104. [[CrossRef](#)]

68. Sousa, C.T.; Nunes, C.; Proenca, M.P.; Leitao, D.C.; Lima, J.L.; Reis, S.; Araujo, J.P.; Lucio, M. pH sensitive silica nanotubes as rationally designed vehicles for NSAIDs delivery. *Colloids Surf. B Biointerfaces* **2012**, *94*, 288–295. [[CrossRef](#)]
69. Tozuka, Y.; Yokohama, C.; Higashi, K.; Moribe, K.; Yamamoto, K. Adsorption state of naphthoic acids on folded sheets mesoporous materials with different pore sizes. *J. Drug Del. Sci. Tech.* **2009**, *19*, 401–404. [[CrossRef](#)]



© 2020 by the authors. Licensee MDPI, Basel, Switzerland. This article is an open access article distributed under the terms and conditions of the Creative Commons Attribution (CC BY) license (<http://creativecommons.org/licenses/by/4.0/>).